Journal of
Marine Science and Engineering

MDPI

Article

Preliminary Feasibility Study of a Magnetic Levitation Rotor Sail for Coastal Area Operations

Kwangseok Lee, Yun Ho Kim, Junghyung Park, Bonggi Choi and Hee Jin Kang *

Alternative Fuels and Power System Research Division, Korea Research Institute of Ships & Ocean Engineering (KRISO), Daejeon 34103, Republic of Korea; kslee@kriso.re.kr (K.L.); yunhokim@kriso.re.kr (Y.H.K.); pjhyung@kriso.re.kr (J.P.); bgchoi@kriso.re.kr (B.C.)
* Correspondence: hjkang@kriso.re.kr; Tel.: +82-42-866-3417

Abstract: The continuous strengthening of environmental regulations is expected to have a significant impact on the vessel operations of shipping companies. Each country must reduce greenhouse gas emissions from ships operating in domestic coastal areas to meet its Nationally Determined Contributions (NDC). For new vessels, we are assessing potential emission reductions through various technologies, recognizing that transitioning to alternative fuels is inevitable to achieve our ultimate goal of zero emissions. However, the introduction of alternative fuels for ships involves numerous challenges, including the overall replacement of propulsion systems, etc. Additionally, to ensure that existing ships can comply with the gradually increasing environmental regulations, the immediate adoption of bridge technologies that can be applied is essential. Rotor sails are recognized as a technology that can be installed on both new ships and vessels in operation, offering carbon emission reductions through thrust assistance. Rotor sails have traditionally been mainly employed on ocean routes with consistent wind patterns. In this paper, we conducted a review of the feasibility of operating rotor sails in coastal areas where wind direction frequently changes and wind intensity is not constant. Particularly, a concept of a rotor sail with magnetic bearings for the rotor sail system, utilizing the principle of magnetic levitation, is suggested. The reduction in frictional forces during rotor sail operation contributes to increased maintainability and advantages in terms of noise and vibration. Specifically, in this study, a structural design for minimizing weight for optimal performance has been carried out.

Keywords: rotor sail; renewable energy; auxiliary propulsion; magnetic bearing; levitation

Citation: Lee, K.; Kim, Y.H.; Park, J.; Choi, B.; Kang, H.J. Preliminary Feasibility Study of a Magnetic Levitation Rotor Sail for Coastal Area Operations. *J. Mar. Sci. Eng.* **2024**, *12*, 32. https://doi.org/10.3390/jmse12010032

Academic Editor: Tie Li

Received: 19 November 2023
Revised: 16 December 2023
Accepted: 17 December 2023
Published: 22 December 2023

1. Introduction

1.1. Previous Studies

The shipping industry is investing in eco-friendly fuels (LNG, CNG, LPG, etc.) and renewable energy technologies (hydrogen, ammonia, solar photovoltaic and thermal energy, wind power, etc.) to reduce reliance on fossil fuels, the primary source of carbon emissions. Wind power, in particular, has garnered significant attention as the most accessible energy source during ocean voyages [1]. Various research studies have explored the use of wing sails [2,3], airborne wind turbines [4,5], wind kites [6,7], rotor sails [8–15], and other methods as auxiliary propulsion systems for ships.

The rotor sail, initially proposed in the 1920s, is a green technology that utilizes the Magnus effect to generate thrust from the pressure difference caused by fluid interaction with a rotating rotor [8]. This technology has been evaluated to achieve fuel savings of over 5% according to the Energy Efficiency Design Index (EEDI) recommended by the International Maritime Organization (IMO) as an energy-saving evaluation criterion [10]. Consequently, extensive research has been conducted on rotor sails, including investigations into cylinder geometry [11–13], rotor–rotor interaction [14], control conditions [15,16], and more. Table 1 shows key findings of previous study for rotor sail.

Table 1. Key findings of previous study for rotor sails.

Research Topic	Key Findings	References
The 'Magnus effect'—the principle of the Flettner rotor	The Magnus effect consists in the fact that a revolving body moving relatively to the surrounding fluid (air) is subjected not only to drag but also to a lift.	A. Betz, 1925 [8]
Analyzing the kinematics of rotor sails	The rotor sail can effectively create large amounts of lift from wind speeds that attack the sail at a range of angles and require very little fuel consumption to generate power.	A. Glatz, 2021 [9]
A parametric study for a Flettner rotor in standalone condition using CFD	CFD-based performance prediction and the parametric study of a Flettner rotor in standalone conditions are validated against wind tunnel results, informed design considerations, and efficiency evaluations	C.S. Kwon et al., 2022 [11]
Flettner rotor concept for marine applications: a systematic study	The performance of a Flettner rotor sail on a tanker ship has been analyzed, with the characterization of lift and drag coefficients.	A. D. Marco et al., 2016 [13]
Aerodynamic interaction on the performance of two Flettner rotors	A Flettner rotor aerodynamic interaction is generally detrimental, and proper trimming of Flettner rotor velocity ratios can attenuate detrimental effects.	G. Bordogna et al., 2020 [14]
Analysis of Flettner rotor ships in beam waves	The influence of Flettner rotors on the roll motion of ships in beam waves is observed using a CFD program, and the one-degree-of-freedom nonlinear roll motion equation is used for roll damping analysis.	H. I. Copuraoglu and E. Pesman, 2018 [15]
The use of Flettner rotors in efficient ship design	Creating a software model for Flettner rotors on UK fleet ships offers initial insights into fuel reduction potential and practical considerations.	D. R. Pearson, 2014 [16]

Most of the research on rotor sails focuses on large-sized ships and long-distance voyages, which can effectively harness wind power and are significantly influenced by weather conditions and scale. This is because the irregularity of the wind and low wind speeds in coastal areas make it challenging to maximize the efficiency of rotor sails. Furthermore, the vibrations and noise resulting from the size and weight of rotor sails pose significant obstacles to their application on coastal vessels.

In line with the goal of reducing fuel consumption and embracing carbon neutrality, the Korea Research Institute of Ships & Ocean Engineering (KRISO) is developing a prototype of a rotor sail based on levitation and magnetic bearing technology. The prototype is a scale model for coastal operation performance evaluation. The prototype has dimensions of 1.5 m in width and 9 m in height, serving as an auxiliary propulsion system that harnesses wind energy.

When utilizing magnetic bearings and the principle of levitation for rotor sail operation, careful consideration is essential for loads imposed on the rotor sail due to wind. Particularly, controlling sudden external load changes is crucial to preventing collisions within the rotating structure and internal components of the rotor sail. Additionally, the weight of the rotor should be reduced to a minimum to minimize power consumption associated with the application of magnetic bearings and the principle of magnetic levitation. Therefore, in this paper, conceptual designs of Radial Magnetic Bearings (RMB) and Axial Magnetic Bearings (AMB) applicable to the prototype are developed. Basic control algorithms are also suggested. Additionally, the Finite Element Method (FEM) presents an approach that minimizes the rotational weight in a scenario where the rotor sail is driven with a configured RMB and AMB. Then, a preliminary feasibility assessment for operational effectiveness in the Korean coastal area is conducted.

1.2. Initial Design Concept

Figure 1 illustrates the external appearance (a) and specifications (b), as well as the internal structural configuration (c), of the rotor sail under consideration in this study. Performance evaluation based on the fundamental specifications of the rotor sail was confirmed through preliminary research using Computational Fluid Dynamics (CFD) techniques [11].

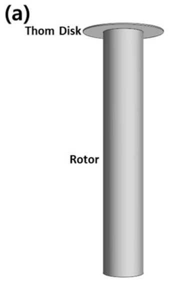

(b)

Quantity	Symbol	Value	Unit
Rotor height	H	9	m
Rotor diameter	D	1.5	m
Aspect ratio	AR	6	-
Thom disk diameter	De	3	m
Diameter ratio	De/D	2	-
*Thom disk thickness	T	0.0375	m
Wind velocity	Vw	8	m/s
**Spin ratio	SR	4	-
Rotor revolution	ω	800	rpm
		83.78	rad/s
Density of air at 25 °C	ρ_{air}	1.184	kg/m^3
Kinematic viscosity of air at 25 °C	ν_{air}	1.567×10^{-5}	m^2/s
Reynolds number	Re	7.66×10^5	-

*Thom disk thickness: **Assumed**
**Spin ratio = $\frac{v_{rotor}}{v_w}$
v_{rotor} = Rotor surface velocity

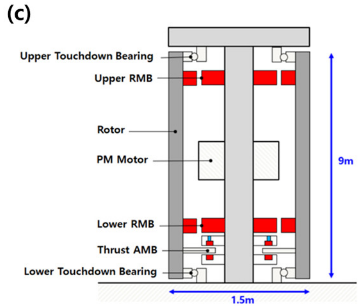

Figure 1. (**a**) The external appearance, (**b**) specification, and (**c**) schematics of the rotor sail with magnetic bearing.

A previous version of this paper was introduced as a proceeding at the 10th PAAMES and studied in more detail. These findings contribute to the development of a structurally stable rotor sail model for coastal passenger ships and provide insights into the expected performance during coastal navigation [17].

In addition to the content presented at the 10th PAAMES, this paper explores design alternatives from the perspective of a magnetic bearing design for the development of a rotor sail utilizing magnetic bearings and the principle of magnetic levitation. After examining these alternatives, we present considerations and structural design results for the development of a lightweight rotor. Finally, we introduce the results of an operational feasibility assessment based on meteorological information from the Korean coastal area.

2. Design Alternatives

2.1. Magnetic Bearings

To maintain a high-speed rotating rotor in a non-contact state, the appropriate load for magnetic bearings must be calculated. The wind load for the magnetic bearing design was considered as follows.

The wind load analysis considers both rotational and non-rotational situations of the rotor sail. The non-rotational scenario represents the ship being anchored. Due to a storm forecast, ships are prohibited from leaving the harbor. Therefore, the structural stability is assessed under a wind speed of 25 m/s, corresponding to the typhoon warning, acting on the rotor frame. The load applied to the non-rotational rotor sail due to wind load, denoted as 'F_{air}' is calculated using Bernoulli's principle in Equation (1):

$$F_{air} = \frac{1}{2} \times \rho_{air} \times A \times {V_{app}}^2 \tag{1}$$

where ρ_{air} is the density of air, assumed to be 1.225 at 15 °C; A is the projected area of the rotor; and V_{app} is the wind velocity acting on the rotor. In the case of rotation, a wind speed of 16 m/s was assumed to calculate the stability of the rotor sail. This wind speed corresponds to the high surf advisory that imposes restrictions on departure. The rotational speed was determined by applying a speed ratio (SR) of 4 to maximize the efficiency of the rotor sail. A lift coefficient of 9.383 and a drag coefficient of 2.863 were employed [16] to calculate the loads exerted by lift and drag during rotor rotation, according to Equations (2) and (3).

$$F_{lift} = \frac{1}{2} \times C_l \times \rho_{air} \times A \times {V_{app}}^2 \tag{2}$$

$$F_{drag} = \frac{1}{2} \times C_d \times \rho_{air} \times A \times {V_{app}}^2 \quad (3)$$

where C_l and C_d represent the lift and drag coefficients of the rotor, respectively.

The rotational torque is analyzed by dividing it into constant and acceleration sections. In the case of constant rotation, the stress applied to the rotor frame is calculated as shown in Equations (4) and (5).

$$(\sigma_r)_{max} = \frac{3+v}{8} \times \rho \times \omega^2 \times (R_{out} - R_{in})^2 \quad (4)$$

$$(\sigma_t)_{max} = \frac{\rho \times \omega^2}{4} \times \left[(3+v) \times {R_{out}}^2 + (1-v) \times {R_{in}}^2\right] \quad (5)$$

Here, v represents the Poisson's ratio of GFRP, assumed to be 0.25, and ρ denotes the density of GFRP, assumed to be 2500 $\mathrm{kg/m^3}$. The rotational angular velocity, ω, is calculated considering a high surf advisory of 16 m/s and a speed ratio of 4. When the wind speed reaches 16 m/s, the apparent wind speed (V_{app}) acting on the rotor, while sailing at a velocity of 6 knots, can reach up to 19 m/s. Additionally, when employing a rotor diameter of 1.5 m, the rotational speed exceeds 720 rpm. To ensure stability, an angular velocity of 83.78 rad/s, corresponding to 800 rpm, was employed. R_{in} and R_{out} represent the inner and outer diameters of the rotor, respectively. Since there is no force in the z direction, the von Mises stresses (σ_V) for the radial (r), tangential (t), and axial (z) directions are determined using Equation (6):

$$\sigma_V = \sqrt{{\sigma_r}^2 + {\sigma_t}^2 + {\sigma_z}^2} \quad (6)$$

In case of acceleration, the torque force (T) applied on the rotor frame is calculated as shown in Equation (7):

$$T = Ia \quad (7)$$

where I is the moment of inertia of the rotor and a is the angular acceleration. The mass of the rotor was calculated by substituting the density of Glass-Fiber-Reinforced Plastic (ρ), while the moment of inertia is defined using Equation (8):

$$I = \frac{1}{2} \times M \times \left({R_{in}}^2 + {R_{out}}^2\right) \quad (8)$$

where M represents the mass of the rotor, which is calculated by multiplying the volume of the rotor by its density (ρ). To ensure appropriate power and stability of the motor, the angular acceleration was set to 8.378 $\mathrm{rad/s^2}$, assuming a maximum speed attainment time of 10 s.

When considering the wind load and rotational torque acting on the rotor sail, it is determined that the applied RMB for the prototype should be able to withstand a maximum load of 6000 N. Accordingly, the RMB applied to the prototype is designed with a straight-fill structure, considering manufacturability, and the coil arrangement and key structures are depicted in Figure 2.

The AMB must withstand the vertical load from the rotor sail's own weight and the vertical acceleration of the ship's movement. Inadequate load capacity may lead to collisions and damage between the support base and rotor sail. Simultaneously, a trade-off between power consumption for AMB operation and the drift generated via the rotor sail should be achieved to maximize efficiency. In this study, considering the prototype specifications, an AMB capable of handling a maximum load of 2100 N (=212 kgf) is designed. The AMB is configured in a form that combines electromagnets (EM) and permanent magnets (PM) to minimize power consumption. The key specifications are illustrated in Figure 3.

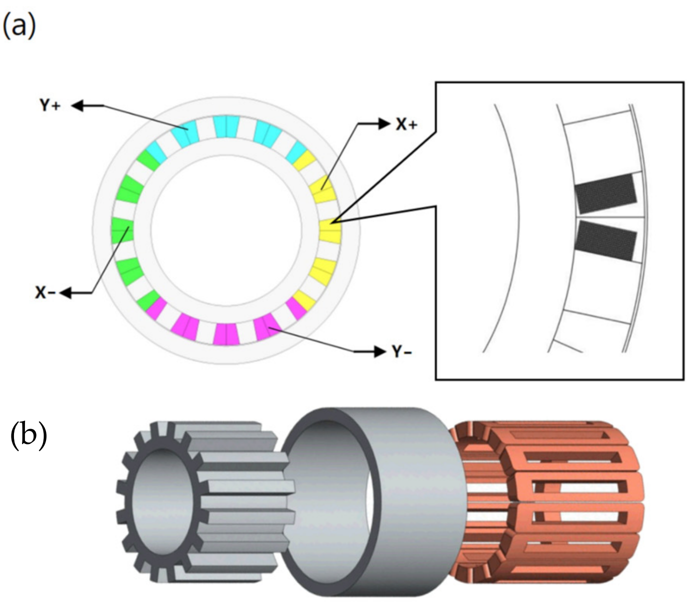

(c)

Parameter	Value
Stator radius (mm)	105.7
Core radius (mm)	131.1
Pole radius (mm)	161.3
Journal radius (mm)	162.5
Rotor radius (mm)	188
Pole width (mm)	25.4
Axial length (mm)	210
Number of poles	16
Number of turns per pole	120
Inductance per axis (mH)	644

Figure 2. The design results of the RMB capable of withstanding a load of 6000 N: (**a**) coil arrangement distribution for x, y-direction control, (**b**) straight-fill structure (∅0.7), and (**c**) derived design parameters.

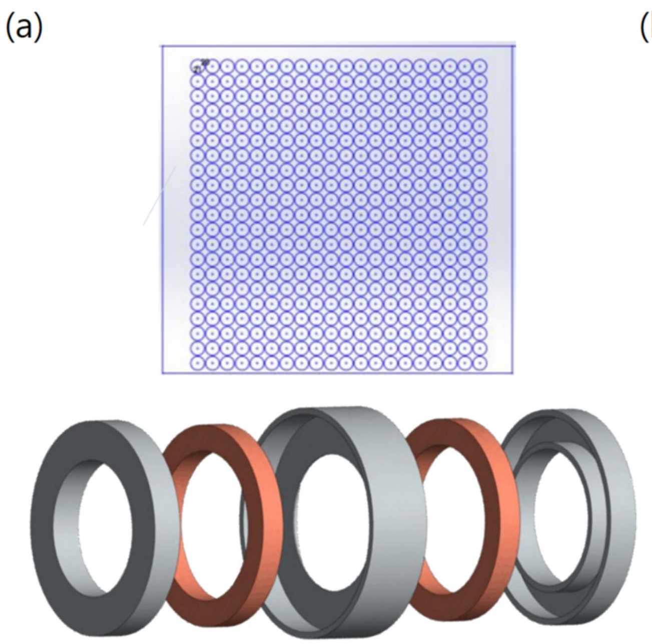

(b)

Parameter	Value
Stator outor radius (mm)	165
Stator inner radius (mm)	105
Coil width (mm)	40
Air gap (mm)	2
Core height (mm)	37.5
Coil height (mm)	47.5
Coil turns	420
Coil diameter (mm)	1.6
Rotor outer radius (mm)	214.5
Inductance (mH)	346

Figure 3. The design results of the AMB capable of withstanding a load of 2100 N: (**a**) coil arrangement (∅1.6) and (**b**) derived design parameters.

The designed RMB and AMB each exhibit electromagnetic forces in the horizontal (x-direction) and vertical (z-direction) distances, as shown in Figure 4. The RMB has a magnetic flux density of 1.5 T at a maximum current of 10 A. Considering electromagnetic forces based on current and gap, it is determined that a current of 4–6 A is appropriate. For the AMB, the analysis of magnetic field control at a maximum current of 10 A reveals similar force characteristics in the up and down coils. To support the load of the rotating rotor, a current of 5 A is deemed suitable. Figure 4 illustrates the electromagnetic forces based on the distances for the designed RMB and AMB.

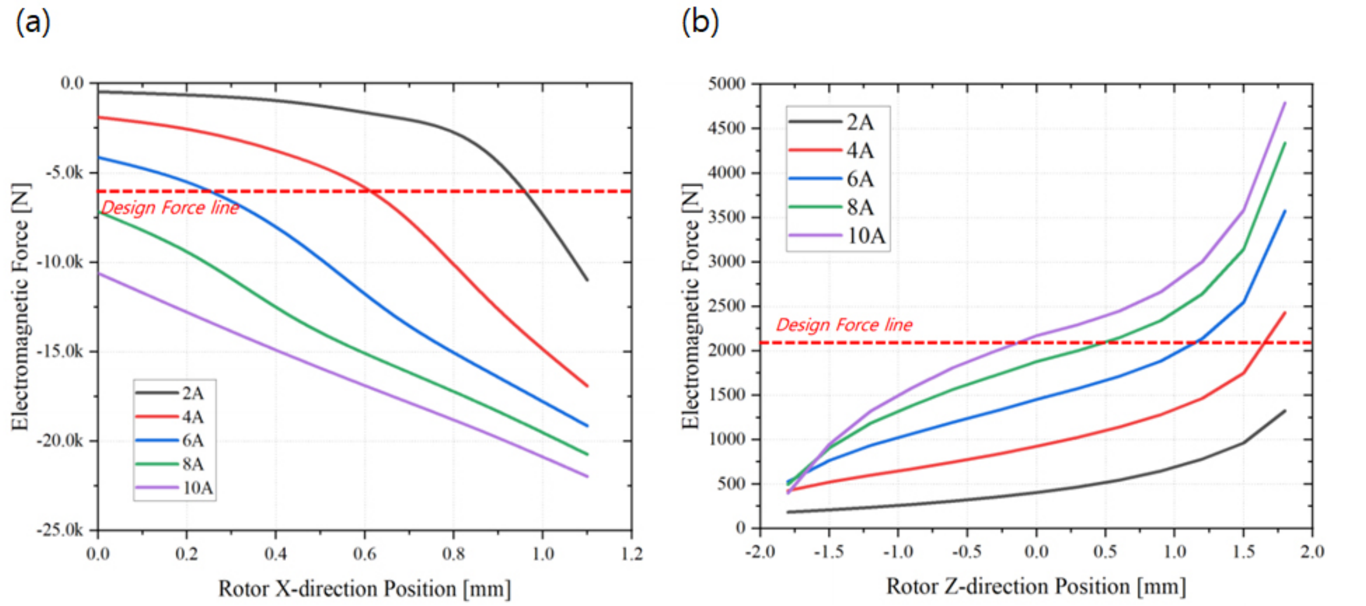

Figure 4. Electromagnetic force characteristics based on rotor position (**a**) for RMB and (**b**) for AMB.

2.2. Lightweight Structure Rotor Design

Several conditions need to be considered for the theoretical analysis of the prototype structure design. The wind interacting with the rotor sail is assumed to be an incompressible and ideal flow fluid to estimate and calculate the Magnus effect. Since the rotor sail will be applied to a magnetic bearing, frictional forces between the rotor sail and the bearing are neglected. The SR, defined as the ratio of the rotor's rotational speed to the wind speed acting on the rotor, is set to 4, which has been identified as the optimal point of efficiency compared to rotational speed [11,15,16]. It is assumed that the rotor sail should be controlled to maintain the speed ratio as the wind speed changes.

The schematic design of the rotor sail is illustrated in Figure 5. The rotor sail, with dimensions of 1.5×9 m^2, incorporates RMB and AMB, with the rotor frame being rotated using a permanent magnet (PM) motor.

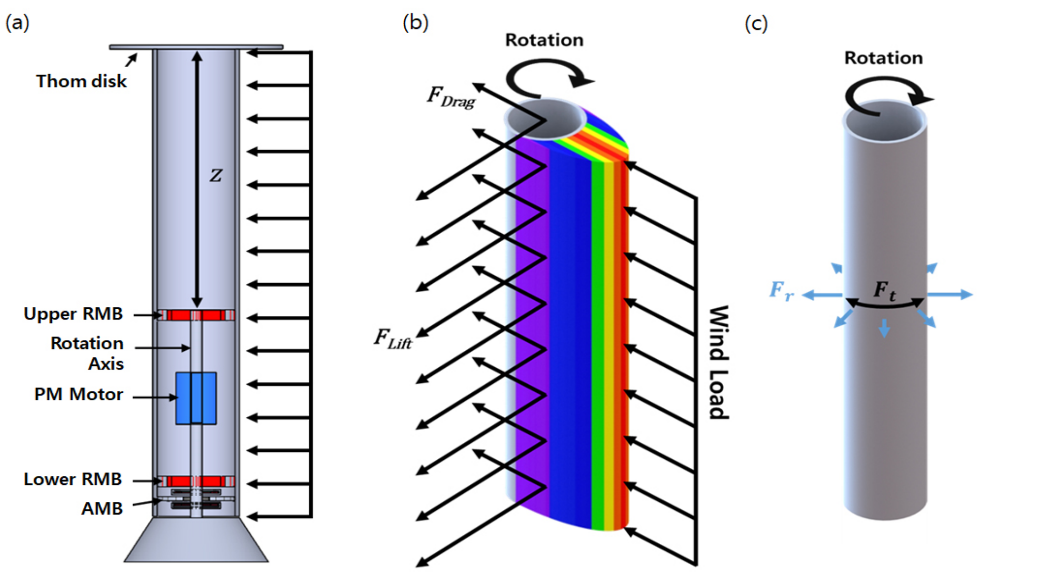

Figure 5. (**a**) Design of rotor sail applied to magnetic bearing, (**b**) distribution of wind load and its lift and drag force, and (**c**) direction of force in torque situation.

Commercial rotor frames typically consist of sandwich-structured composite materials made of GFRP/Carbon-Fiber-Reinforced Plastic (CFRP) and polyurethane (PU) foam [18]. GFRP/CFRP is used for the outer wall, while polyurethane foam serves as the core material. Considering the external forces experienced during ocean navigation, the commercial frames are estimated to have a composite thickness of 8 mm. When making a judgment about structural strength, we put in an S.F. of 3.0 to see if this value exceeds the structural strength.

In this paper, we assumed and examined the rotor design, considering the load capacity of magnetic bearings. Additionally, we considered the design of a lightweight rotor structure to minimize power consumption for rotor sail propulsion while withstanding wind load and rotational torque. With a GFRP rotor of 2 mm thickness, a size of approximately 1.5 m by 9 m results in a weight of about 212 kg. This weight seems suitable considering the load capacities of 6000 N for RMB and 2100 N for AMB. However, further verification is needed to assess whether it can withstand wind load and rotational torque at a level of approximately one-fourth compared to the typical thickness of commercial rotors, which is 8 mm.

Given the thinness of the frame, a single material is used instead of a sandwich-structured composite. GFRP, which has lower strength compared to CFRP, is selected as the material for a thorough stability analysis.

The structural stability of the rotor sail is analyzed using the ANSYS 2022 R1 static structural module in both non-rotational and rotational situations. Since the lower RMB is positioned above the AMB, the position of the lower RMB is fixed. Subsequently, the stress and deformation of the rotor frame are analyzed based on the position (z) of the upper RMB. The mesh for the FEM analysis is created in a hexahedral shape for the rotor frame, while the endplate is generated in a tetrahedral shape based on the rotor frame, as shown in Figure 6. The total number of elements used is 98,471. When a wind load compresses the rotor frame, the RMB provides internal support for the rotor frame. Since the RMB prevents the deformation of the rotor frame, the corresponding parts are set as fixed supports.

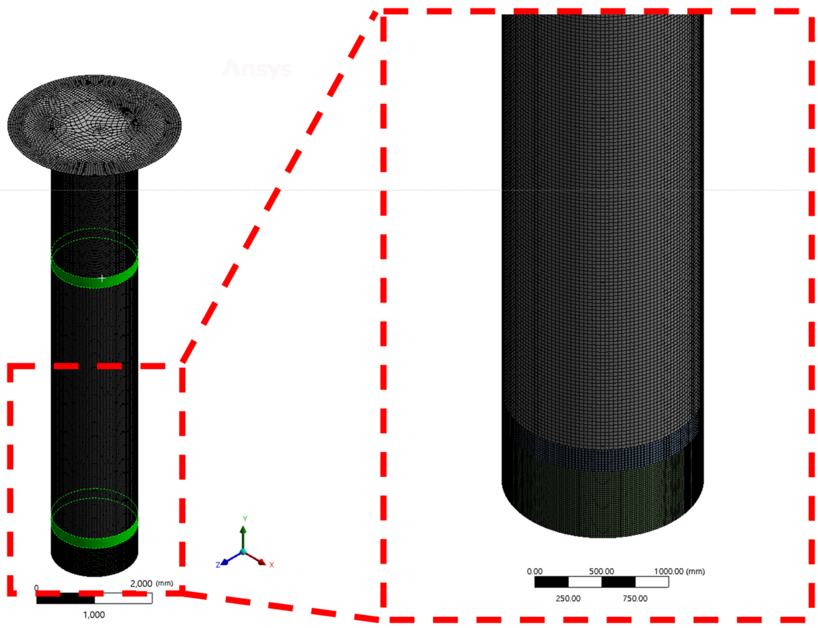

Figure 6. Generated mesh for wind load situation.

Figure 7a illustrates the distribution of stress and deformation resulting from wind loads in a non-rotational situation, simulated through FEM analysis. The position of the upper RMB significantly affects stress and deformation. Notably, the point (*z*/*H*) corresponding to 20% exhibits the minimum stress, while the minimum deformation occurs at the 40% location (Figure 7c). Even in rotation, the distribution of stress and deformation tends to exhibit similar patterns (Figure 7b).

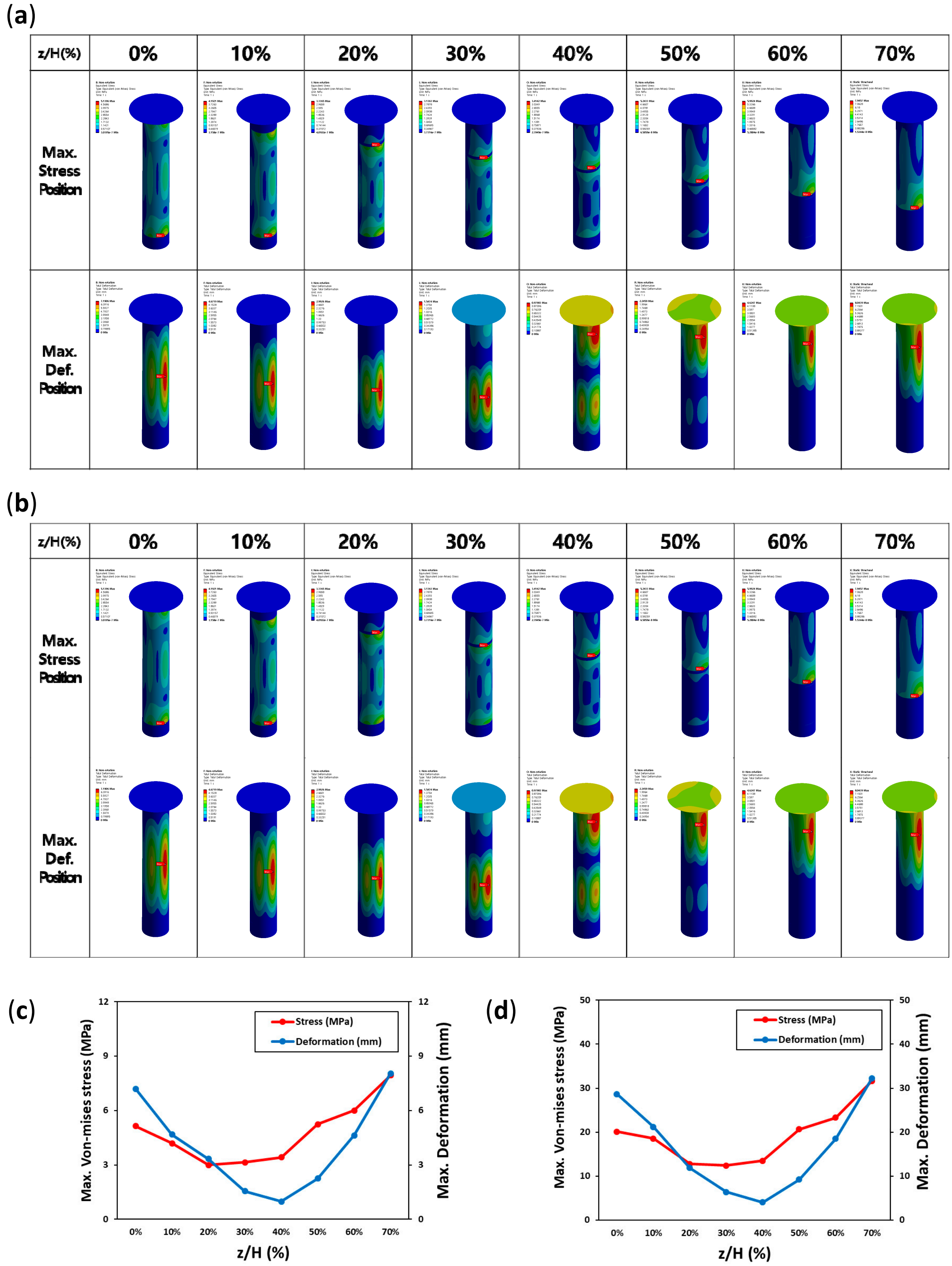

Figure 7. The distribution of stress and deformation with the *z/H* ratio using FEM in cases of (**a**) non-rotation and (**b**) rotation, maximum von Mises stress, and deformation with upper RMB distance ratio in cases of (**c**) non-rotation and (**d**) rotation.

Typically, it is expected that minimum stress and subsequent deformation occur when the upper RMB is centered. However, our observations reveal that the minimum stress is concentrated within the 20–40% range. This phenomenon arises due to deformation resulting from external forces acting on an object. When the deformation is constrained by a fixed support, stress becomes concentrated instead of being uniformly distributed. Consequently, while the deformation of the rotor frame limited by the fixed support decreases, the stress intensifies rather than diminishes.

Regarding deformation, it was confirmed that the least deformation occurs near the point where the difference in cross-sectional area between the upper and lower rotor frames of the upper RMB is minimized, given that the lower RMB is fixed at a distance of 600 mm from the bottom. Furthermore, as the rotor frame situated above the upper RMB experiences significant deformation, it becomes influenced by the weight of the endplate. Consequently, the position of the maximum stress shifts from the bottom to the top.

In the case of non-rotation, the maximum stress occurs when the rotor frame at the top of the upper RMB reaches 70%, resulting in a stress value of 7.945 MPa. During rotation, the maximum stress value is 31.653 MPa.

The structural stability of the rotor sail was analyzed using the ANSYS static structural module under acceleration conditions. The FEM analysis employed a mesh configuration, as illustrated in Figure 8. The mesh consists of hexahedral elements surrounding the rotor, totaling 36,264 elements. When torque is applied during rotor rotation, it induces tension on the rotor, rendering the support provided by the RMB ineffective. Therefore, the mesh was generated without subdividing the parts.

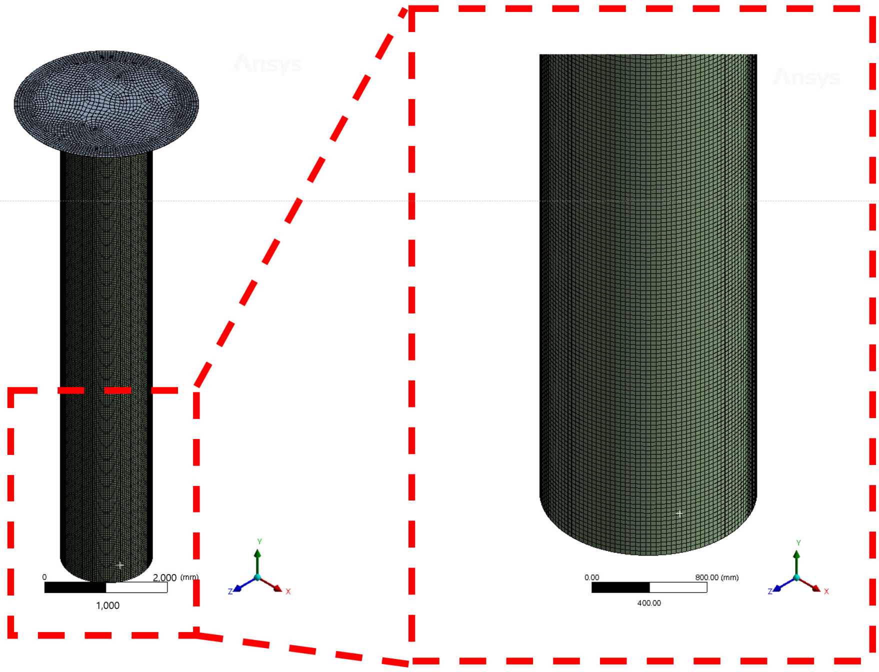

Figure 8. Generated mesh for torque situation.

Figure 9 presents the results of the FEM analysis, illustrating the stress and deformation caused by torque applied to the rotor frame under maximum acceleration conditions (a = 8.378 rad/s^2). Since the upper section is constrained by the endplate, while the lower part is free, the highest stress is observed in the region where deformation is restricted, as previously mentioned. In summary, torque during maximum acceleration induces a stress of 0.15144 MPa. The torque applied during the rotational motion at a constant maximum speed is calculated as the maximum stress of 9.86 MPa using Equations (4)–(6).

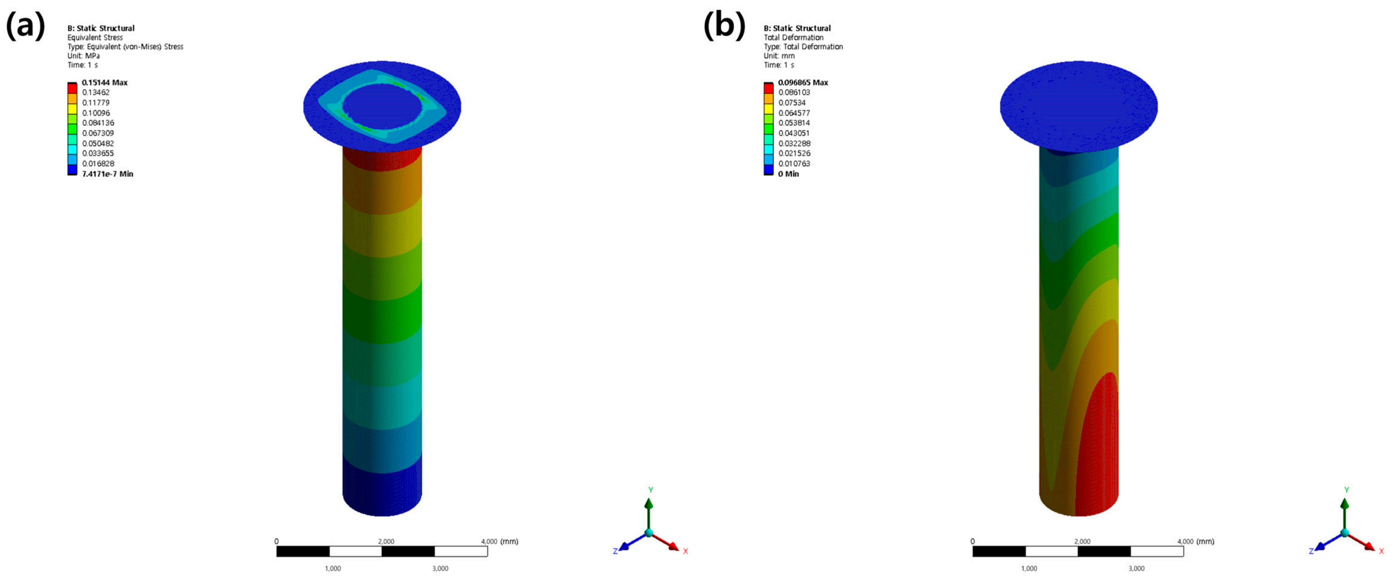

Figure 9. The distribution of (**a**) stress and (**b**) deformation with acceleration condition.

2.3. Examination of Structural Stability Applied on D.A.F.

Table 2 presents stress data resulting from wind loads and torque, categorized based on the x/H ratio, for the assessment of rotor sail stability. Since rotational conditions tend to produce higher stresses compared to non-rotational ones, the wind load values are specifically provided for the rotational scenario. To account for the maximum load application on the rotor sail, all loads were aggregated, and a dynamic amplification factor (D.A.F.) of 3.0 was applied. Despite the use of a D.A.F. of 3.0, the stress values remain below the maximum tensile strength of 593 MPa and bending strength of 760 MPa for the rotor frame. This confirms the structural stability of the rotor sail with a 2 mm thickness.

Table 2. Examination of structural stability applied on D.A.F. 3.0 in rotational situation.

z/*H* Ratio	Wind Load (MPa)	Torque (MPa)		Total (MPa)	Applied D.A.F. 3.0
		Acceleration	Constant		
0%	20.61	0.15	9.86	30.62	91.86
10%	16.21	0.15	9.86	26.22	78.66
20%	12.27	0.15	9.86	22.28	66.84
30%	11.09	0.15	9.86	21.10	63.30
40%	16.58	0.15	9.86	26.59	79.77
50%	25.36	0.15	9.86	35.37	106.11
60%	28.66	0.15	9.86	38.67	116.01
70%	37.50	0.15	9.86	47.51	142.53

3. Operational Suitability Assessment of the Prototype in Coastal Areas

3.1. Target Ship

In this study, a 30-ton class demonstration ship was chosen as the target vessel to incorporate a rotor sail. The ship's design is depicted in Figure 10, and its specifications are provided in Table 3.

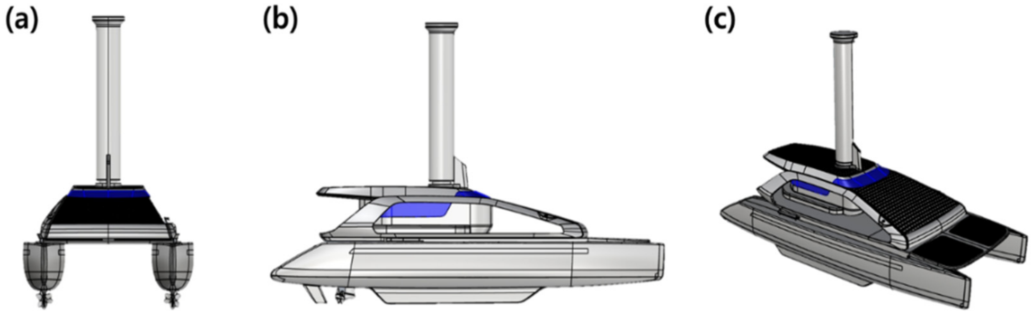

Figure 10. The design concept of the 30-ton class demonstration ship (Vinssen Co., Ltd., Yeongam, Korea, Designed): (**a**) front view, (**b**) side view, and (**c**) isometric view.

Table 3. Design specification of 30-ton class demonstration ship.

Parameter	Value	Unit
Length Over All (L.O.A.)	25	m
Breadth	8.5	m
Height	16.5	m
Draft	0.7	m
Displacement	Abt. 30	ton
Speed	Max. 10	knots
Motor Power	50 × 2	kW
Hull Materials	Aluminum/FRP	–

3.2. The Methods of Assessment for Preliminary Performance

To analyze the preliminary performance of a 1.5 × 9 m^2 rotor sail, we made assumptions about the route and weather conditions. For route selection, three routes were chosen, representing departures from three major harbors in the Republic of Korea, as illustrated in Figure 11. Two routes (① Incheon–Jeju and ② Busan–Jeju), characterized by their relatively long distances and differing directions (Figure 11a), were selected for the initial performance assessment. Additionally, a route (③ Hyanghwa–Songi) with a relatively shorter distance (Figure 11b) was also included.

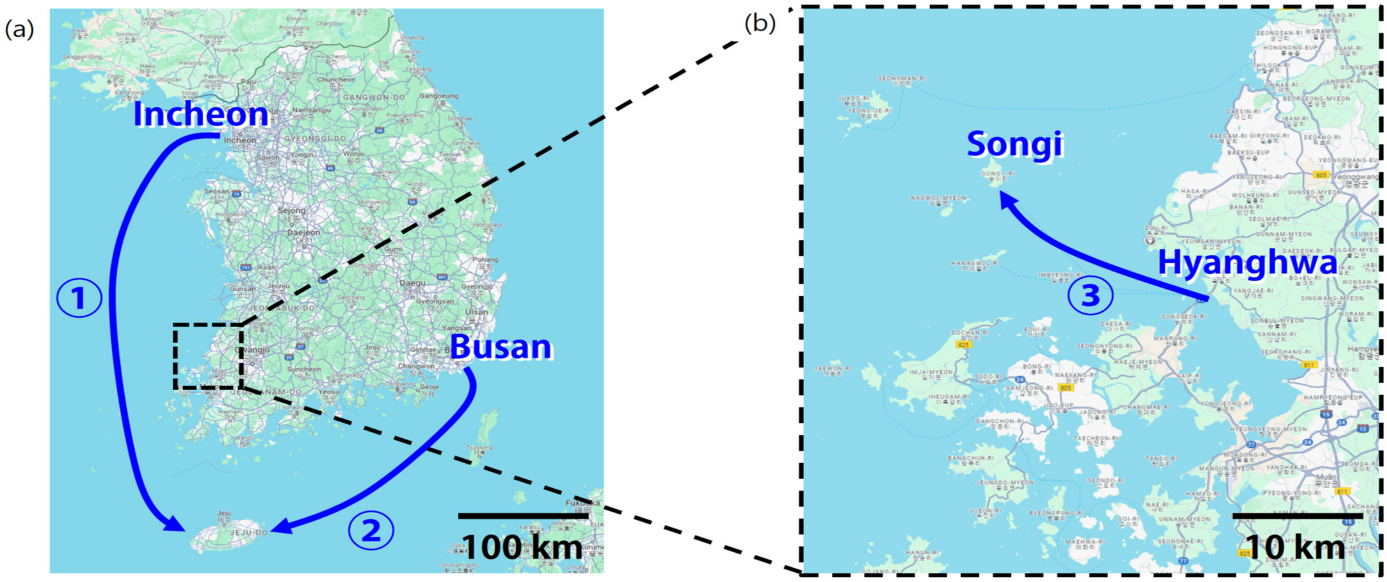

Figure 11. The routes of (**a**) Incheon–Jeju/Busan–Jeju and (**b**) Hyanghwa–Songi for analyzing the preliminary performance of the rotor sail.

Segments were categorized based on the ship's navigational direction obtained from the selected routes (Table 4). The initial performance was estimated by inputting wind direction and wind speed data into these segments. Meteorological data for the chosen routes were obtained from a data buoy positioned along the routes (Figure 12). Hourly data recorded over the course of a year (from 1 September 2021 to 31 August 2022) during coastal passenger operation hours (7:00 a.m.–5:00 p.m.) were utilized. Equation (8) was employed to calculate the thrust exerted on the rotor sail when subjected to wind. In Equation (8), x is the wind direction.

$$\begin{aligned} F_{thrust} &= F_{lift}\cos\left(\tfrac{\pi}{2} - x\right) + F_{drag}\cos(x)\ (x > 0) \\ &= F_{lift}\sin(x) + F_{drag}\cos(x) \\ &= \tfrac{1}{2} \times \rho_{air} \times A \times {V_{app}}^2 \times (C_l\sin(x) + C_d\cos(x)) \end{aligned} \tag{9}$$

Table 4. Routes for the preliminary performance test of the rotor sail.

Routes		Average Wind Speed	Buoy No.	Navigational Direction (Deg)
①	Segment 1	17.7 knots	1	228.46
	Segment 2		2	200.32
	Segment 3		3	182.03
	Segment 4		4	178.88
	Segment 5		4	159.39
	Segment 6		4	122.38
②	Segment 1	13.4 knots	8	124.07
	Segment 2		8	216.22
	Segment 3		7	236.77
	Segment 4		6	240.05
③	Segment 1	10.9 knots	5	285.41
	Segment 2		5	287.48
	Segment 3		5	301.09
	Segment 4		5	318.47

Figure 12. Location of ocean data buoy.

Moreover, the thrust exerted by the rotor sail based on wind speeds of 8 m/s and sailing at 6 knots, according to the wind direction, can be depicted as shown in Figure 13.

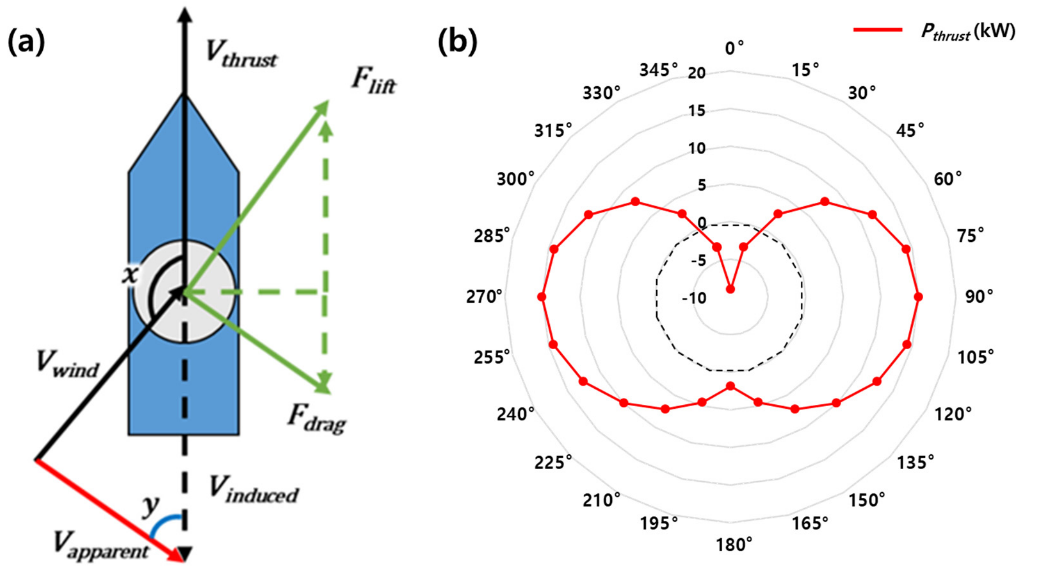

Figure 13. (**a**) A schematic diagram of the rotor sail's thrust by applying wind force. (**b**) The graph of thrust for gaining rotor sail with wind direction (V_{app} = 8 m/s, V_{thrust} = 6 knots).

3.3. Seasonal Meteorological Data Obtained from Buoys

Seasonal meteorological data measured using buoys are presented in Figures 14 and 15. We only present the graph for buoy ⑤ because the data from the other buoys exhibited similar and repetitive patterns. The selected route areas exhibit distinct wind directions and speeds based on prevailing westerlies and seasonal influences.

Figure 14 provides a representation of wind frequency categorized by season, revealing a higher frequency of north winds in all seasons except summer, where south winds prevail. Based on these observations, it is predicted that segments along the equatorial horizontal direction would offer optimal conditions for harnessing the propulsive power of the rotor sail within the selected area. However, upon analyzing Figure 15, it becomes apparent that higher wind speeds are predominantly concentrated in the north wind direction.

As a result, it is inferred that the most efficient propulsion can be achieved when sailing in the southwest or southeast direction, taking into account both the lift and drag forces generated via the Magnus effect. To assess the rotor sail's thrust, buoy data were applied to Equation (8), allowing for the identification of thrust-generating segments ($F_{thrust} > 0$). An SR of 4 was then applied to these segments to maximize efficiency. By summing the calculated F_{thrust} for these segments and dividing by the total number of data points (N), the expected thrust for the auxiliary propulsion of the rotor sail was determined. Multiplying this expected thrust by the sailing speed provides an estimation of the ship's output (P_{avg}), as described in Equation (9):

$$P_{avg} = \frac{\sum_{n=1}^{N} F_{thrust,n}}{N} \cdot V_{ship} \quad \begin{cases} F_{thrust} & if\ F_{thrust} \geq 0; \\ 0 & if\ F_{thrust} < 0. \end{cases} \tag{10}$$

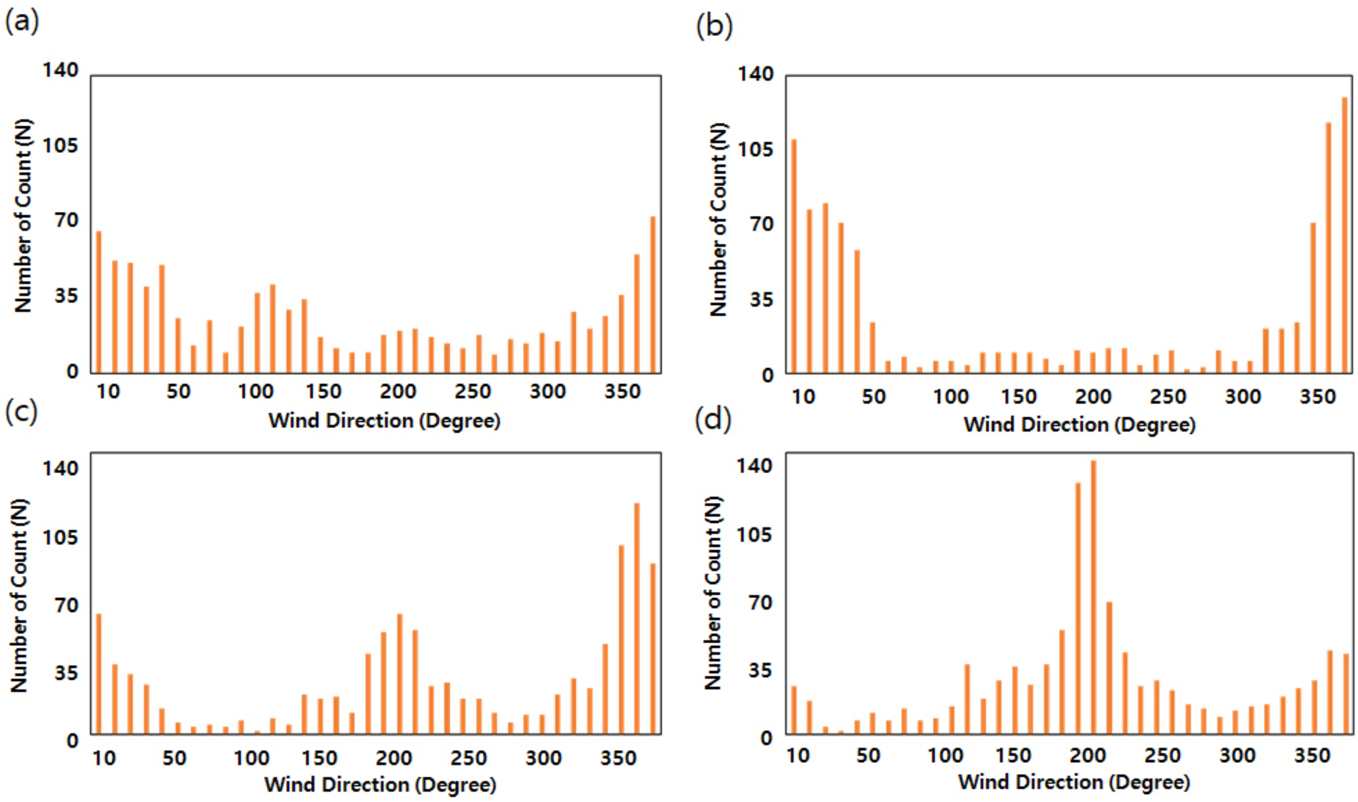

Figure 14. The graph of wind direction frequency in (**a**) fall, (**b**) winter, (**c**) spring, and (**d**) summer in buoy ⑤.

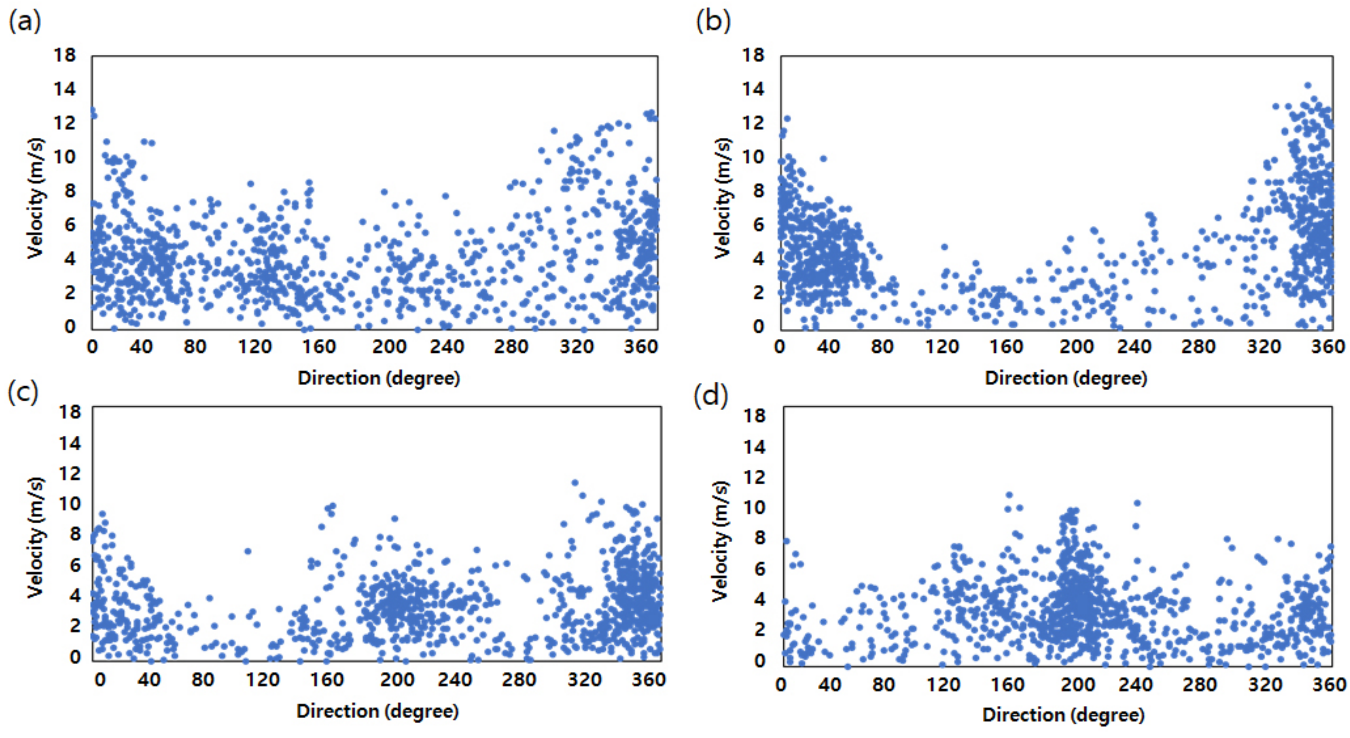

Figure 15. The distribution of wind direction–velocity in (**a**) fall, (**b**) winter, (**c**) spring, and (**d**) summer in buoy ⑤.

3.4. Assessments of Preliminary Performance

Table 5 presents the attainable thrust for different seasons and routes based on the analysis of Figures 14 and 15.

Table 5. Seasonal thrust of rotor sail for routes.

Routes		Average Power (kW)			
		Fall	Winter	Spring	Summer
①	Segment 1	8.171	10.284	3.109	3.337
	Segment 2	7.432	7.110	2.399	2.915
	Segment 3	6.673	6.562	2.226	2.938
	Segment 4	6.159	6.349	2.857	5.540
	Segment 5	6.394	9.008	3.134	3.645
	Segment 6	7.975	14.744	4.867	0.857
②	Segment 1	11.392	10.163	6.287	6.807
	Segment 2	12.308	19.085	6.563	5.369
	Segment 3	7.637	14.772	3.384	3.115
	Segment 4	7.164	11.822	2.238	1.850
③	Segment 1	6.560	12.274	5.250	5.390
	Segment 2	6.452	11.989	5.099	5.319
	Segment 3	5.607	9.457	3.863	4.671
	Segment 4	4.480	5.320	2.302	3.623

Since the prevailing wind direction is predominantly northward, as per the meteorological buoy data, the southward navigation relies on drag force for thrust, while the east–west navigation benefits from the lift force generated via the rotor sail. In a given set of weather conditions, variations in thrust can occur depending on the route direction. Therefore, if a route aligns with the locally dominant wind direction and allows for the acquisition of thrust, the use of a rotor sail may be considered appropriate. Analysis of one year's worth of data from the meteorological buoys indicates that a maximum thrust of 19.085 kW can be achieved. This corresponds to approximately 19% of the propulsion motor output of a 30-ton class demonstration ship, showcasing the potential of rotor sail technology in marine propulsion.

The thrust generated by the rotor sail was calculated as per Equation (11), and the power consumption was calculated with reference to A. Lele (2017) using Equations (12) and (13) [18].

$$P_{thrust} = F_{thrust} \cdot V_{ship} \tag{11}$$

$$P_{cons} = F_{fric} \cdot U_{rot} \tag{12}$$

$$F_{fric} = \left(\frac{0.455}{(log(Re))^{2.58}} - \frac{1700}{Re} \right) \cdot \rho_A \cdot \frac{U_{rot}^2}{2} \cdot A_r \tag{13}$$

Here, U_{rot} represents the rotational speed of the rotor, and it is a variable dependent on the wind speed multiplied by SR. Additionally, ρ_A denotes the density of air, and A_r represents the surface area of the rotor.

The net power is calculated as the difference between thrust and power consumption, as shown in Equation (14).

$$P_{net} = P_{thrust} - P_{cons} \tag{14}$$

In this paper, it is assumed that the designed rotor sail is installed on a 30-ton class demonstration ship for practical demonstration. The considerations for calculating power consumption under this scenario are presented in Table 6.

Table 6. Power consumption calculation parameters.

Parameter	Value
Reynolds number (Re)	5×10^5
Density of air (ρ_A)	1.225 kg/m^3
Surface area of the rotor (A_r)	42.4 m^2
Rotational speed of rotor (U_{rot})	variable

The estimated results for the thrust, power consumption, and net output produced by the 30-ton class demonstration ship, equipped with the rotor sail under KRISO's ship specification, are presented in Figure 16.

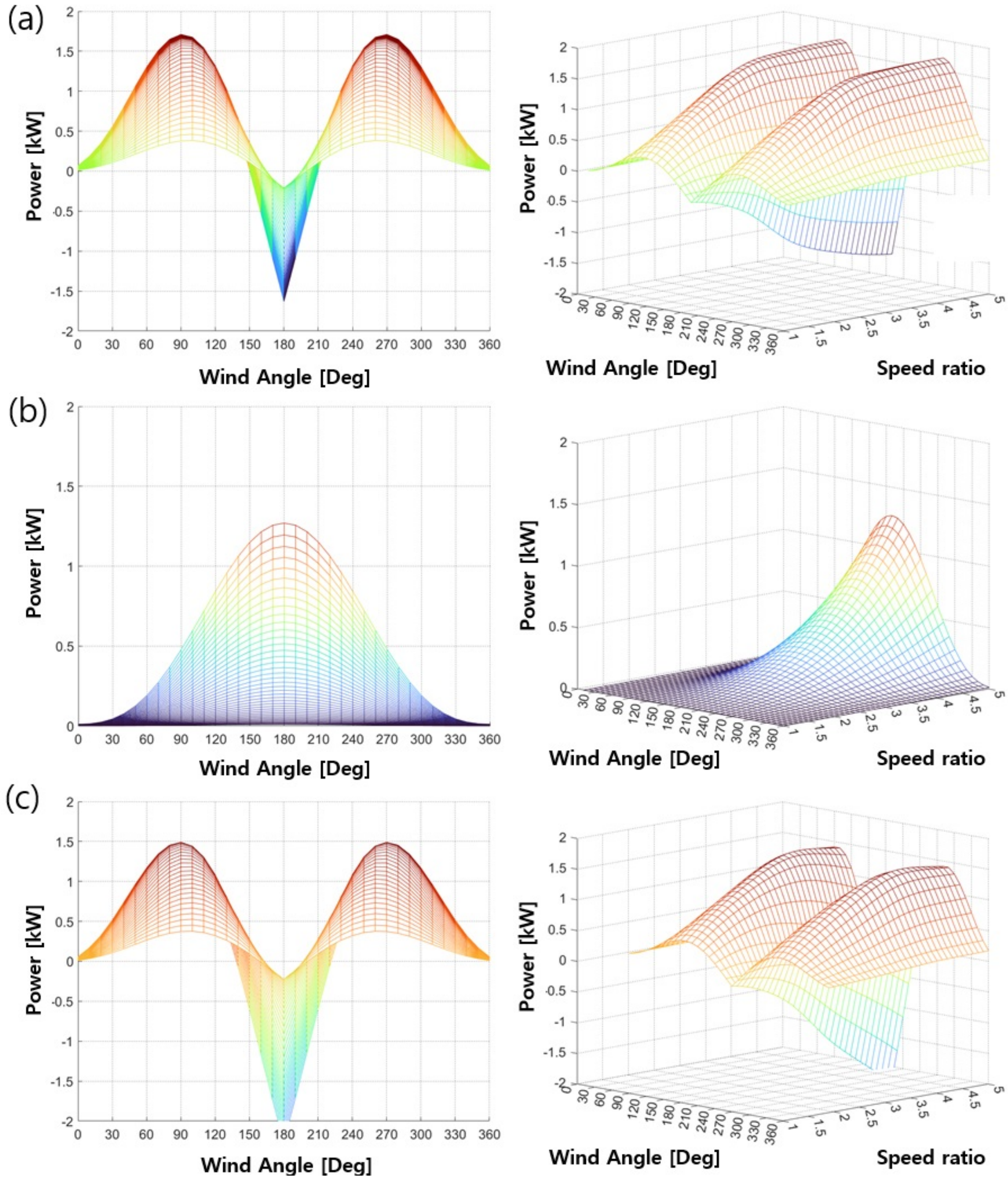

Figure 16. Instantaneous thrust (**a**), consumption (**b**), and net power (**c**) profile at ship speed of 10 knots.

In Figure 16a, it can be observed that the thrust reaches its maximum around 90 and 270 degrees, depending on the wind angle. Meanwhile, in Figure 16b, the consumption peaks at 180 degrees. Figure 16c represents the difference between thrust in Figure 16a and consumption in Figure 16b, emphasizing the importance of reducing the power expended in the rotation of the rotor sail to achieve a more effective operation. While factors influencing the navigation conditions of actual vessels may reduce the utility obtained from simulations, it has been theoretically confirmed that approximately 19 kW of thrust assistance is achievable.

4. Conclusions

In this study, research results on the use of rotor sails in coastal areas for achieving IMO's ship emission GHG regulations and Nationally Determined Contributions (NDC) were presented. Considering the variable wind conditions in coastal areas, a new rotor sail concept utilizing magnetic bearings and the principle of magnetic levitation was proposed, allowing for easy speed control while reducing noise and vibration. A rotor sail configuration incorporating Radial Magnetic Bearings (RMB) and Axial Magnetic Bearings (AMB) was suggested, examining lightweight options based on the designed load capacities of each magnetic bearing. The prototype rotor, designed with a 2 mm thickness of Glass-Fiber-Reinforced Polymer (GFRP), was confirmed to withstand wind loads and rotational torque in Korean coastal regions within the load capacity of the magnetic bearings. Assuming operation on a demonstration ship of approximately 30 m in length and 100 kW power in Korean coastal areas, the prototype could potentially provide an auxiliary thrust of around up to 19 kW. Subsequent research will analyze the relationship between the power required for the prototype's operation and the resulting propulsion power to assess its economic feasibility. Furthermore, plans include the construction of the demonstration ship and the prototype for sea trials in Korean coastal areas, aiming to verify the operability of the rotor sail utilizing magnetic bearings and the principle of magnetic levitation.

Limitation: This paper investigated the initial feasibility of the application of a rotor sail for small- or medium-sized vessels operating in coastal areas of the Republic of Korea. Therefore, lots of technical problems shall be solved before its application in the real world, such as considering actual wind properties (as spectrum or wind profile vertically) rather than constant wind speed, coupling effect of the rotor sail and ship dynamics, considering the actual operating modes of the rotor sail (increment/decrement speed, noise, statistical variations, and so on), etc. Based on our initial issuing, we will continuously develop our research step by step.

Author Contributions: Conceptualization, K.L., J.P., B.C., Y.H.K. and H.J.K.; methodology, K.L. and H.J.K.; software, K.L.; validation, H.J.K. and K.L.; writing—original draft preparation, K.L.; writing—review and editing, H.J.K. All authors have read and agreed to the published version of the manuscript.

Funding: This research was supported by a grant from the "Development of technologies to improve passenger ship efficiency based on renewable energy (1525013857/PMS5480)", the "Development of 1 MW class Marine Test-bed for Adoptability Demonstration of Alternative Fuels (1525012293/PMS5560)", and the "Development of basic technologies to evaluate electric-powered system for in eco-friendly ship & demonstrate ship-applicability of carbon-free fuel (1525013819/PMS5490)" funded by the Ministry of Oceans and Fisheries of Korea.

Institutional Review Board Statement: Not applicable.

Informed Consent Statement: Not applicable.

Data Availability Statement: Data are contained within the article.

Acknowledgments: The authors would like to express their sincere gratitude for the support provided by the Ministry of Oceans and Fisheries, Republic of Korea, as well as the support of Vinssen Co., Ltd.

Conflicts of Interest: The authors declare no conflict of interest.

Abbreviation

AMB	Axial Magnetic Bearings
CFD	Computational Fluid Dynamics
CII	Carbon Intensity Indicator
CNG	Compressed Natural Gass
D.A.F.	Dynamic Amplification Factor
EEDI	Energy Efficiency Design Index
EEXI	Energy Efficiency Existing Ship Index
EM	Electromagnets
FEM	Finite Element Method
GFRP	Glass-Fiber-Reinforced Plastic
IMO	International Maritime Organization
LNG	Liquefied Natural Gas
LPG	Liquefied Petroleum Gas
MEPC	Marine Environment Protection Committee
NDC	Nationally Determined Contributions
PM	Permanent Magnets
RMB	Radial Magnetic Bearings
SR	Speed Ratio

References

1. Lele, A.; Rao, K.V.S. Ship propulsion strategies by using wind energy. In Proceedings of the 2016 International Conference on Emerging Technological Trends (ICETT), Kollam, India, 21–22 October 2016; p. 16726886. [CrossRef]
2. Li, D.; Zhang, Y.; Li, P.; Dai, J.; Li, G. Aerodynamic performance of a new double-flap wing sail. *Pol. Marit. Res.* **2019**, *26*, 61–68. [CrossRef]
3. Li, C.; Wang, H.; Sun, P. Numerical investigation of a two-element wingsail for ship auxiliary propulsion. *J. Mar. Sci. Eng.* **2020**, *8*, 333. [CrossRef]
4. Khan, Z.; Rehan, M. Harnessing airborne wind energy: Prospects and challenges. *J. Control Autom. Electr. Syst.* **2016**, *27*, 728–740. [CrossRef]
5. Santana, D.A.D.; El-Thalji, I. Scalability and compatibility analyses of airborne wind technology for maritime transport. In *IOP Conference Series: Materials Science and Engineering*; IOP Publishing: Bristol, UK, 2019; Volume 700, p. 012064. [CrossRef]
6. Leloup, R.; Roncin, K.; Behrel, M.; Bles, G.; Leroux, J.-B.; Jochum, C.; Parlier, Y. A continuous and analytical modeling for kites as auxiliary propulsion devoted to merchant ships, including fuel saving estimation. *Renew. Energy* **2016**, *86*, 483–496. [CrossRef]
7. Podeur, V.; Merdrignac, D.; Behrel, M.; Roncin, K.; Fonti, C.; Jochum, C.; Parlier, Y.; Renaud, P. Fuel economy assessment tool for auxiliary kite propulsion of merchant ship. *La Houille Blanche* **2018**, *1*, 5–7. [CrossRef]
8. Betz, A. The 'Magnus Effect'—The Principle of the Flettner Rotor. No. NACA-TM-310. 1925. Available online: https://ntrs.nasa.gov/citations/19930086918 (accessed on 11 July 2023).
9. Glatz, A. Analyzing the Kinematics of Rotor Sails. Norsepower. Available online: https://www.researchgate.net/publication/348420252_Analyzing_the_Kinematics_of_Rotor_Sails (accessed on 11 July 2023).
10. IMO Revised GHG Reduction Strategy for Global Shipping Adopted. Available online: https://www.imo.org/en/MediaCentre/PressBriefings/pages/Revised-GHG-reduction-strategy-for-global-shipping-adopted-.aspx (accessed on 11 July 2023).
11. Kwon, C.S.; Yeon, S.M.; Kim, Y.C.; Kim, Y.G.; Kim, Y.H.; Kang, H. A parametric study for a flettner rotor in standalone condition using CFD. *Int. J. Nav. Archit. Ocean. Eng.* **2022**, *14*, 100493. [CrossRef]
12. Marzuki, O.F.; Rafie, A.S.M.; Romli, F.I.; Ahmad, K.A. Magnus wind turbine: The effect of sandpaper surface roughness on cylinder blades. *Acta Mech.* **2018**, *229*, 71–85. [CrossRef]
13. Marco, A.D.; Mancini, S.; Pensa, C.; Calise, G.; Luca, F.C. Flettner rotor concept for marine applications: A systematic study. *Int. J. Rotating Mach.* **2016**, *2016*, 3458750. [CrossRef]
14. Bordogna, G.; Muggiasca, S.; Giappino, S.; Belloli, M.; Keuning, J.A.; Huijsmans, R.H.M. The effects of the aerodynamic interaction on the performance of two Flettner rotors. *J. Wind. Eng. Ind. Aerodyn.* **2020**, *196*, 104024. [CrossRef]
15. Copuraoglu, H.I.; Pesman, E. Analysis of Flettner Rotor ships in beam waves. *Ocean. Eng.* **2018**, *150*, 352–362. [CrossRef]
16. Pearson, D.R. The use of flettner rotors in efficient ship design. In Proceedings of the Influence of EEDI on Ship Design Conference, London, UK, 24–25 September 2014; Available online: https://www.researchgate.net/publication/287081987_The_use_of_Flettner_rotors_in_efficient_ship_design (accessed on 11 July 2023).

17. Lee, K.; Kim, Y.; Choi, B.; Park, J.; Kang, H.J. Study of structural design and initial estimation of flettner rotor for coastal passenger ship of renewable energy. In Proceedings of the 10th Pan Asian Association of Maritime Engineering Societies, Kyoto, Japan, 20 October 2023.
18. Lele, A.; Rao, K.S. Net power generated by flettner rotor for different values of wind speed and ship speed. In Proceedings of the 2017 International Conference on Circuit, Power and Computing Technologies (ICCPCT), Kollam, India, 20–21 April 2017. [CrossRef]